Enhanced half-metallicity of off-stoichiometric quaternary Heusler alloy Co_{2}(Mn,Fe)Si investigated through saturation magnetization and tunneling magnetoresistance

Kidist Moges, Yusuke Honda, Hong-xi Liu, Tetsuya Uemura, Masafumi Yamamoto, Yoshio Miura, and Masafumi Shirai

Enhanced half-metallicity of off-stoichiometric quaternary Heusler alloy Co$_2$(Mn,Fe)Si investigated through saturation magnetization and tunneling magnetoresistance

Kidist Moges, Yusuke Honda, Hong-xi Liu, Tetsuya Uemura,

and Masafumi Yamamoto[*]

[1] *Division of Electronics for Informatics, Graduate School of Information Science and Technology, Hokkaido University, Sapporo 060-0814, Japan*

Yoshio Miura

[2] *Electrical Engineering and Electronics, Kyoto Institute of Technology, Kyoto 606-8585, Japan*

Masafumi Shirai

[3] *Research Institute of Electrical Communication, Tohoku University, Sendai 980-8577, Japan*

[*]yamamoto@nano.ist.hokudai.ac.jp

Abstract

We investigated the factors that critically affect the half-metallicity of the quaternary Heusler alloy $Co_2(Mn,Fe)Si$ (CMFS) by examining the film composition dependence of the saturation magnetization per formula unit, μ_s, of CMFS thin films and the TMR ratio of CMFS/MgO/CMFS magnetic tunnel junctions (MTJs). We also investigated the origin of the giant TMR ratio of up to 2610% at 4.2 K (429% at 290 K) obtained for CMFS MTJs with Mn-rich, lightly Fe-doped CMFS electrodes. The lower μ_s than that of the half-metallic Z_t-24 and the lower TMR ratio for (Mn+Fe)-deficient CMFS than for (Mn+Fe)-rich CMFS were consistently explained by Co antisites at the nominal Mn/Fe sites. It was revealed that the $Co_{Mn/Fe}$ antisite is detrimental to the half-metallicity of CMFS quaternary alloy, as it is in Co_2MnSi ternary alloy. It was also shown that (Mn+Fe)-rich compositions are critical to suppressing these harmful antisites and to retaining the half-metallic electronic state. In addition, a relatively small Fe ratio rather than a large one in the total (Mn+Fe) composition led to a more complete half-metallic electronic state. Half-metallicity was more strongly enhanced by increasing the Mn composition in Mn-rich, lightly Fe-doped CMFS than in Mn-rich Co_2MnSi. This phenomenon is the cause of the giant TMR ratio recently reported for CMFS MTJs. Our findings indicate that the approach to controlling off-stoichiometry and film composition is promising for fully utilizing the half-metallicity of quaternary CMFS thin films as spin source materials.

I. INTRODUCTION

The creation of a highly spin-polarized current is essential for spintronic devices that are expected to have characteristics of nonvolatility, reconfigurable logic functions, and low power consumption [1,2]. Originating from the existence of an energy gap at the Fermi level (E_F) for one spin direction (mostly the minority-spin band), half-metallic ferromagnets (HMFs) feature complete spin polarization at E_F [3]. Accordingly, HMFs are seen as one of the most suitable spin source materials for spintronic devices. Co-based Heusler alloys (Co$_2YZ$, where Y is usually a transition metal and Z is a main group element) [4] are among the most extensively applied to spintronic devices, including magnetic tunnel junctions (MTJs), in particular those with a MgO barrier [5−12], and giant magnetoresistance (GMR) devices [13−18], and to spin injection into semiconductors [19−25]. This is due to the theoretically predicted half-metallicity for many of them [26−28] and their high Curie temperatures, which are well above room temperature (RT) [29].

In practice, off-stoichiometry in Co$_2YZ$ thin films prepared by magnetron sputtering or molecular beam epitaxy is inevitable and leads to structural defects. If the minority-spin in-gap states are introduced at E_F by a structural defect for a half-metallic or nearly half-metallic film, the half-metallicity is strongly degraded. Thus, it is important to understand the effect of defects associated with off-stoichiometry on half-metallicity in order to take full advantage of the half-metallic character of Co-based Heusler alloys. Here, experiments and first-principles calculations have identified harmful defects affecting the half-metallicity of Co$_2$MnSi (CMS) and Co$_2$MnGe (CMG), i.e., Co antisites at nominal Mn sites (Co$_{Mn}$ antisites) [8,30,31]. The effect of these antisites has been studied in terms of the tunneling magnetoresistance (TMR) ratio [8−10,31], saturation magnetization per formula unit [8,31], and surface spin polarization [32]. Moreover, the electronic states of off-stoichiometric CMS and CMG films have been investigated by high-energy x-ray photoelectron spectroscopy [33−35] and the magnetic states by x-ray absorption spectroscopy and x-ray magnetic circular dichroism [36−38]. These studies have indicated that the harmful Co$_{Mn}$ antisites can be suppressed with a Mn-rich composition. In particular, by suppressing these harmful antisites, high TMR ratios of up to 1995% at 4.2 K and up to 354% at 290 K have been demonstrated for fully epitaxial CMS/MgO/CMS MTJs (CMS MTJs) having Mn-rich CMS electrodes [10].

One of the notable advantages of Co-based Heusler alloys is that they feature a variety of materials, including not only ternary alloys but also quaternary alloys, thereby providing flexibility in their application to spintronic devices. One quaternary Heusler alloy system Co$_2$(Mn$_{1−x}$Fe$_x$)Si has been studied from the viewpoint of tuning the E_F position around the center of the half-metal gap by changing the composition x in Co$_2$(Mn$_{1−x}$Fe$_x$)Si in order to control the valence electron number per formula unit, Z_t [39−45]. It has also been used to make spintronic devices, including Co$_2$(Mn,Fe)Si/AlO$_x$-based MTJs [46] and GMR devices [17,18]. Large magntoresistance ratios at room temperature have been demonstrated for Co$_2$(Mn$_{0.6}$Fe$_{0.4}$)Si/Ag/Co$_2$(Mn$_{0.6}$Fe$_{0.4}$)Si GMR devices [17,18].

We recently investigated the influence of off-stoichiometry on the TMR characteristics of fully epitaxial Co$_2$(Mn,Fe)Si (CMFS)/MgO/CMFS MTJs (CMFS MTJs) with Co$_2$Mn$_{\alpha'}$Fe$_{\beta'}$Si$_{0.84}$ electrodes [47]. We showed that the TMR ratios at 4.2 K and 290 K of the

MTJs significantly increased when the (Mn+Fe) composition δ (= $\alpha'+\beta'$) was increased from a δ-deficient composition to a δ-rich one while keeping a constant α' value of 0.73 (series-A CMFS MTJs). This result was explained by using the antisite-based site-specific formula unit composition model for the quaternary CMFS and assuming that Co antisites at the nominal Mn/Fe sites are detrimental to the half-metallicity [47] on the basis of findings obtained for the ternary CMS [31]. Furthermore, we demonstrated giant TMR ratios of 2610% at 4.2 K and 429% at 290 K for the MTJ with lightly Fe-doped, Mn-rich CMFS ($Co_2Mn_{1.24}Fe_{0.16}Si_{0.84}$) electrodes through the Fe composition (β') dependence of the TMR ratio of CMFS MTJs having $Co_2(Mn_{\alpha'}Fe_{\beta'})Si_{0.84}$ electrodes with a constant ($\alpha'+\beta'$) value of 1.40 (series-B CMFS MTJs) [47]. These TMR ratios are significantly higher than those obtained for CMS MTJs having Mn-rich CMS electrodes [10]. However, the origin of the giant TMR ratio obtained for CMFS MTJs with lightly Fe-doped, Mn-rich CMFS electrodes has yet to be fully understood.

The purpose of the present study was twofold: (i) to clarify the effect of off-stoichiometry on the half-metallicity of quaternary Heusler alloy CMFS and (ii) to clarify the origin of the enhanced half-metallicity for lightly Fe-doped, Mn-rich CMFS electrodes indicated by the giant TMR ratios. To do this, we experimentally investigated the film composition dependence of the saturation magnetization per formula unit, μ_s, of CMFS films with various compositions of α' and β' in $Co_2(Mn_{\alpha'}Fe_{\beta'})Si_{0.84}$ in combination with first-principles calculations. Furthermore, in order to clarify the key factor that determines the film composition dependence of the TMR ratio with a different approach from those for series-A and series-B CMFS MTJs, we experimentally investigated how the TMR ratio of CMFS MTJs with lightly Fe-doped CMFS electrodes depends on the Mn composition α' in $Co_2(Mn_{\alpha'}Fe_{0.16})Si_{0.84}$ electrodes in the Mn-rich composition region (series-C CMFS MTJs). To take account of defects arising from off-stoichiometry in CMFS in the first-principles calculations, we used the antisite-based site-specific formula unit composition (SSFU) model for the quaternary alloy CMFS which was originally developed for the ternary alloy CMS.

This paper is organized as follows. Section II details the experimental and computational methods. This section also describes how the SSFU composition model for off-stoichiometric ternary CMS is extended to include off-stoichiometric quaternary CMFS. Section III presents the results and discusses them. Section III A investigates the effect of off-stoichiometry on the half-metallicity of the quaternary Heusler alloy $Co_2(Mn,Fe)Si$ through the δ dependence of μ_s of $Co_2Mn_{0.73}Fe_{\beta'}Si_{0.84}$ thin films having compositions ranging from δ-deficient to δ-rich. The experimental dependences of μ_s and the TMR ratio of CMFS MTJs on δ are discussed in terms of the effect of defects associated with off-stoichiometry on the electronic states identified by the first-principles calculations. Accordingly, it is shown that a δ-rich composition is essential to retaining the half-metallicity of the quaternary alloy as it suppresses the detrimental $Co_{Mn/Fe}$ antisites as in a similar way as in the ternary alloy. Section III B describes the origin of the giant TMR ratio of CMFS MTJs with Mn-rich, lightly Fe-doped CMFS. The β' dependence of μ_s for δ-rich CMFS films with a fixed δ composition (δ = 1.40) was experimentally investigated and compared with the results of the first-principles calculations. The δ dependence of the TMR ratio of the MTJs with Mn-rich, lightly Fe-doped (β' = 0.16) CMFS electrodes was also experimentally investigated by varying α'. The enhancement in the TMR ratio for the MTJ with $Co_2Mn_{1.24}Fe_{0.16}Si_{0.84}$

4

electrodes (δ = 1.40) of up to 2610% at 4.2 K and μ_s being close to its half-metallic value can be explained by the half-metallicity being retained for δ-rich CMFS with a small amount of Fe replacing Mn, wherein residual Co$_{Mn/Fe}$ antisites are further suppressed by the δ-rich composition. Section IV summarizes our results and concludes the paper.

II. EXPERIMENTAL AND COMPUTATIONAL METHODS

A. Experimental methods

Epitaxial CMFS thin films with various Mn and Fe compositions, α' and β', were prepared for investigating the effect of off-stoichiometry on μ_s. The layer structure of all the thin films prepared for the magnetization measurements was, from the substrate side, MgO buffer (10 nm)/Co$_2$Mn$_{\alpha'}$Fe$_{\beta'}$Si$_{0.84}$ (~30 nm)/MgO barrier (2 nm)/AlO$_x$ cap layer (1 nm) grown on a (001)-oriented MgO single crystalline substrate. This layer structure corresponds to half of a MTJ. Two series of films with different values of α' and β' in Co$_2$Mn$_{\alpha'}$Fe$_{\beta'}$Si$_\beta$ (β = 0.84) were prepared. In the series-A films, α' was fixed at 0.73 while β' was varied from 0 to 0.67 (Table I). Thus, the (Mn+Fe) composition, $\delta = \alpha' + \beta'$, in series A was varied from a δ-deficient composition, δ = 0.73, to a δ-rich composition, δ = 1.40 (a δ-deficient composition in CMFS corresponds to $\delta < 2-\beta$, while δ-rich corresponds to $\delta > 2-\beta$). On the other hand, in the series-B films, α' and β' were systematically varied while δ was fixed to a δ-rich value of 1.40; i.e., β' (α') was varied from β' = 0 to 0.67 (from α' = 1.40 to 0.73) (Table II). These two series of thin films correspond to the electrodes in the series-A and series-B CMFS MTJs reported in Ref. 47, respectively.

The CMFS thin film was deposited at RT using radio-frequency magnetron cosputtering from three targets, i.e., nearly stoichiometric Co$_2$MnSi, Mn, and Fe, in an ultrahigh vacuum chamber (having a base pressure of 6×10^{-8} Pa) and was subsequently *in situ* annealed at 600°C for 15 min. to improve the atomic ordering. α' and β' in Co$_2$Mn$_{\alpha'}$Fe$_{\beta'}$Si$_{0.84}$ were systematically varied by adjusting the relative amounts of sputtered Mn and Fe. The MgO barrier was deposited as a protection layer of the CMFS film because the interface between CMS, CMG, or CMFS with a MgO barrier have high-quality structural [47], electronic, and magnetic properties [33−38,48−50]. The MgO buffer and barrier were deposited by electron beam evaporation in the same chamber at 400°C and RT, respectively. After depositing the MgO barrier, the sample was transferred to another ultrahigh-vacuum chamber (through an ultrahigh vacuum), and an Al metallic layer (1 nm) was deposited by electron beam evaporation. After that, the AlO$_x$ cap was prepared by exposing the Al layer to an O$_2$ atmosphere of ~ 1×10^5 Pa for 2 h. The film composition of the prepared CMFS film was determined by inductively coupled plasma analysis with an accuracy of 2%−3% for each element except Si, for which the accuracy was 5%.

The CMFS layers grown on MgO-buffered MgO(001) substrates were characterized by making reflection high-energy electron diffraction (RHEED) observations during growth. We made in situ observations of the RHEED patterns for each successive layer of the MgO buffer/CMFS (30 nm) heterostructures. Sharp streak patterns depending on the electron injection direction were obtained for each successive layer, clearly indicating that the CMFS layer grew epitaxially on a MgO-buffer. These results were consistent with those of the

5

structural characterization by aberration-corrected Z-contrast scanning transmission electron microscopy for a CMFS lower electrode grown on a CoFe buffer layer and a CMFS upper electrode grown on a MgO tunnel barrier in a fully epitaxial MTJ with $Co_2Mn_{1.24}Fe_{0.16}Si_{0.84}$ electrodes: both consisted of $L2_1$ regions and B2 regions [47].

The magnetic properties of the two series of CMFS films were investigated using a superconducting quantum interference device (SQUID) at 10 K. The saturation magnetization for the total volume of each film, M_s, at 10 K was estimated by extrapolation of the obtained M-H curve to $H = 0$ to subtract the contribution from the MgO substrate. Figures 1(a) and (b) show the M-H curve of series-A and series-B CMFS films. In order to determine μ_s from the obtained M_s of each CMFS film, the film thickness was precisely measured by using a low-angle x-ray reflectivity (XRR) technique. For all the films, clear oscillations in the experimental reflectivity scan were observed up to $2\theta \sim 7^o$, indicating smooth interfaces and surface. A fit of the oscillatory XRR intensity for a 2θ range from 1.4 to 5.6° was used to determine the thickness of each $Co_2Mn_{\alpha'}Fe_{\beta'}Si_{0.84}$ layer. We also determined the in-plane, a, and out-of-plane, c, lattice constants of each series of films, including the CMS films, by making x-ray Bragg scans with a four-axis x-ray diffractometer (Bruker AXS D8 Discover Hybrid) equipped with a scintillation counter (Table I and Table II) and incorporated these values in the determination of μ_s.

Finally, in order to further elucidate the film composition dependence of the TMR ratio of CMFS MTJs, we prepared series-C CMFS MTJs having the following layer structure: (from the substrate side) MgO buffer (10 nm)/$Co_{50}Fe_{50}$ (CoFe) buffer (30 nm)/$Co_2Mn_{\alpha'}Fe_{0.16}Si_{0.84}$ lower electrode (3 nm)/MgO barrier (1.4−3.2 nm)/$Co_2Mn_{\alpha'}Fe_{0.16}Si_{0.84}$ upper electrode (3 nm)/CoFe (1.1 nm)/$Ir_{22}Mn_{78}$ (IrMn) (10 nm)/Ru cap (5 nm), grown on a MgO (001) single-crystal substrate. The preparation of the series-C CMFS MTJs was essentially the same as that of the previously reported series-A and series-B CMFS MTJs [47], except that the series-C CMFS thin films were the upper and lower electrodes, where the series-C CMFS ($Co_2Mn_{\alpha'}Fe_{\beta'}Si_{0.84}$) had a fixed β' of 0.16 and α' ranging from 1.14 to 1.24. Briefly, each layer was successively deposited in an ultrahigh vacuum chamber (with a base pressure of about 6 × 10^{-8} Pa). The $Co_2(Mn,Fe)Si$ electrodes were prepared by co-sputtering from nearly stoichiometric Co_2MnSi, Mn, and Fe targets. We fabricated the MTJs by photolithography and Ar ion milling. The junction size was 10×10 μm². The magnetoresistance was measured using the dc four-probe method. The TMR characteristics of the MTJs were measured at a bias voltage of 5 mV at 290 K and 1 mV at 4.2 K. We defined the TMR ratio as $(R_{AP}-R_P)/R_P$, where R_{AP} and R_P are the resistances for the antiparallel (AP) and parallel (P) magnetization configurations between the upper and lower electrodes. The TMR curves at 4.2 K and 290 K of the series-C CMFS MTJ with $Co_2Mn_{1.24}Fe_{0.16}Si_{0.84}$ electrodes (t_{MgO} = 2.9 nm), which was also included in the series-B CMFS MTJs and reported in [47], exhibited clear exchange-biased TMR characteristics along with giant TMR ratios of 2610% at 4.2 K and 429% at 290 K. Typical minor-loop TMR curves for the fabricated MTJs showed that the tunneling resistances R_P and R_{AP} were almost constant against the magnetic field [47]. Accordingly, the error of the TMR ratio, defined as $(R_{AP}-R_P)/R_P$, was less than about 2% for each junction. Figure 2 plots typical dependences on t_{MgO} of R_PA, $R_{AP}A$, and the TMR ratio at 290 K for these MTJs over a t_{MgO} range from 2.2 to 3.0 nm, where A is the junction area. The

6

dependences of $R_\mathrm{p}A$ and $R_\mathrm{AP}A$ on t_MgO were exponential, with almost identical slopes in log(RA) over the whole plotted range. Moreover, the almost identical slopes resulted in nearly constant TMR ratios from 2.2 to 3.0 nm of t_MgO. Accordingly, the standard deviation of the TMR ratio obtained for the MTJs was about 3%. These results indicate that the TMR characteristics of the MTJs fabricated on a 20×20 mm^2 substrate had good reproducibility.

B. Computational method

We performed first-principles density functional calculations to theoretically investigate the effect of off-stoichiometry in Co$_2$(Mn,Fe)Si on the electronic and magnetic states on the basis of the Korringa-Kohn-Rostoker (KKR) method [52,53] with the coherent potential approximation (CPA) for atomic disorder. The generalized gradient approximation (GGA) was used for the exchange and correlation term [54]. We theoretically evaluated the total spin magnetic moments per formula unit, m_spin, the spin-resolved, local density of states (LDOS), and spin polarizations at E_F for three series of CMFS: (1) series A and (2) series B, described in Sec. III A and III B, and (3) series C of Co$_2$(Mn$_{\alpha'}$Fe$_{0.16}$)Si$_{0.84}$ with a fixed β' of 0.16 in Co$_2$(Mn$_{\alpha'}$Fe$_{\beta'}$)Si$_{0.84}$ and α' ranging from α' = 1.14 (δ = 1.30) to 1.24 (δ = 1.40). We used a scalar relativistic calculation, in which the spin-orbit interaction was neglected. 8000 points were included in the full Brillouin zone (BZ) for the BZ integration. The unit cell of the full-Heusler alloy X_2YZ with the $L2_1$ structure consists of four different fcc sublattices. Each has an atom basis as follows: X element at (1/4,1/4,1/4) and (3/4,3/4,3/4), Y at (0,0,0), and Z at (1/2,1/2,1/2). We used the experimental lattice constants a described above for series-A (Table I), series-B (Table II), and series-C (Table III) CMFS, but ignored the small difference between a and c, assuming a cubic lattice with the experimental a value for each film. The calculations were based on the SSFU composition model assuming antisite formation rather than vacancy formation to accommodate off-stoichiometry, as described in Sec. II C.

C. Formula unit composition model

The site-specific formula unit compositions for off-stoichiometric Co-based Heusler alloys are essential to understanding the effect of off-stoichiometry on their half-metallicity. We have proposed an antisite-based site-specific formula unit (SSFU) composition model for the ternary Heusler alloys Co$_2$MnSi and Co$_2$MnGe, which assumes the formation of only antisite defects, not vacancies, to accommodate off-stoichiometry [8,31]. The basis for this assumption is the theoretically predicted higher formation energies of vacancies compared with those of antisite defects for Co$_2$MnSi [27,55]. We extended this model to off-stoichiometric quaternary Co$_2$(Mn$_{\alpha'}$Fe$_{\beta'}$)Si$_\beta$ by assuming that the Mn to Fe ratio is constant for all nominal Mn/Fe, Si, and Co sites. According to this model, each site in the $L2_1$ structure is occupied either by the nominal atom (Co, Mn/Fe or Si for CMFS) for that site or by an antisite defect atom, so the total number of atoms included in the formula unit is always four, even though the film is off-stoichiometric in terms of the Co:Mn/Fe:Si atomic ratio. Thus, this model preserves a generalized 2:1:1 stoichiometry in terms of the site occupancy.

Given this assumption, the role of δ = α'+β' for the quaternary CMFS is identical to α for the ternary CMS expressed as Co$_2$Mn$_\alpha$Si$_\beta$ in terms of the determination of the SSFU

composition type. Accordingly, the SSFU composition types developed for off-stoichiometric ternary $Co_2Mn_\alpha Si_\beta$ ($0 < \alpha < 2$ and $0 < \beta < 2$) [31] can be applied to off-stoichiometric quaternary $Co_2(Mn_{\alpha'}Fe_{\beta'})Si_\beta$ ($0 < \delta < 2$ and $0 < \beta < 2$) by replacing α in $Co_2Mn_\alpha Si_\beta$ with $\delta = \alpha'+\beta'$ for quaternary $Co_2(Mn_{\alpha'}Fe_{\beta'})Si_\beta$. This is because we can rewrite the empirical expression of $Co_2(Mn_{\alpha'}Fe_{\beta'})Si_\beta$ as $Co_2[(Mn_{1-\xi}Fe_\xi)]_\delta Si_\beta$ and thus make a direct correspondence between α and δ. The resultant general expressions for the SSFU composition types of type I to type IV are shown in Table IV. Here, the Mn to Fe ratio, $1-\xi : \xi$, in the general expressions of the SSFU compositions is given by the α' to β' ratio in the expression of $Co_2(Mn_{\alpha'}Fe_{\beta'})Si_\beta$. (Note that the expression of $Co_2(Mn_{\alpha'}Fe_{\beta'})Si_\beta$ is an empirical one for a film composition in which each atomic composition is expressed with respect to Co_2.) In addition to the previously introduced type I to type III SSFU compositions [31], we introduced composition type IV for the region of $\beta > (2+\delta)/3$ and $\delta > 2-\beta$ in order to extend the generality of the antisite-based SSFU composition model.

Tables I, II, and III respectively show the calculated SSFU compositions for CMFS series A ($Co_2(Mn_{0.73}Fe_{\beta'})Si_{0.84}$) with a fixed α' of 0.73 and various β' ranging from 0 ($\delta = 0.73$) to 0.67 ($\delta = 1.40$), series B ($Co_2(Mn_{\alpha'}Fe_{\beta'})Si_{0.84}$) with a constant δ of 1.40 and various α' and β' ranging from $\alpha' = 0.73$ ($\beta' = 0.67$) to $\alpha' = 1.40$ ($\beta' = 0$), and series C ($Co_2(Mn_{\alpha'}Fe_{0.16})Si_{0.84}$) with a fixed β' of 0.16 and various α' ranging from 1.14 ($\delta = 1.30$) to 1.24 ($\delta = 1.40$). All films of series A, B and C fall into type II or type III SSFU compositions, where type II contains $Co_{Mn/Fe}$ antisites, while type III contains no $Co_{Mn/Fe}$ antisites. The Z_t-24 value for each film composition is also shown for series-A to series-C CMFS films, where Z_t is the valence electron number per formula unit. The Z_t-24 values for off-stoichiometric CMFS films are those given by the antisite-based SSFU composition model. Note, however, that the same values can be obtained by assuming that each formula unit contains four atoms along with antisites, not vacant sites, to accommodate off-stoichiometry without specifying the site occupation [47].

III. RESULTS AND DISCUSSION

A. Effect of off-stoichiometry on half-metallicity of quaternary Heusler alloy $Co_2(Mn,Fe)Si$

First, we describe the effect of off-stoichiometry through the film composition dependence of μ_s of series-A CMFS films, i.e., $Co_2Mn_{\alpha'}Fe_{\beta'}Si_{0.84}$ with $\alpha' = 0.73$ and that of the TMR ratio of series-A CMFS MTJs.

Figure 3(a) plots the experimental μ_s at 10 K for series-A CMFS as a function of δ ranging from $\delta = 0.73$ ($\beta' = 0$, $Co_2Mn_{0.73}Si_{0.84}$) to 1.40 ($\beta' = 0.67$, $Co_2Mn_{0.73}Fe_{0.67}Si_{0.84}$) along with the Z_t-24 values. A much lower μ_s than the Z_t-24 value was observed for $\delta = 0.73$ ($\beta' = 0$) film, i.e., a Mn-deficient CMS film. This result has been explained by the deviation from half-metallicity due to the existence of Co_{Mn} antisites for Mn-deficient CMS [31]. Importantly, by increasing the Fe composition β', μ_s increased and got closer to the Z_t-24 value with increasing δ from $\delta = 0.73$ ($\beta' = 0$) to 1.30 ($\beta' = 0.57$), and μ_s for $\delta = 1.30$ ($\beta' = 0.57$) was in good agreement with the half-metallic value, Z_t-24. This dependence of μ_s on δ in the range from $\delta = 0.73$ ($\beta' = 0$) to 1.30 ($\beta' = 0.57$) was very similar to the dependence of μ_s on the Mn

8

composition α in off-stoichiometric $Co_2Mn_\alpha Si$ films [31]. On the other hand, a further increase in δ from $\delta = 1.30$ ($\beta' = 0.57$) to 1.40 ($\beta' = 0.67$) resulted in a distinctly lower μ_s than its Z_t–24 value, indicating a deviation from half-metallicity in $Co_2Mn_{0.73}Fe_{0.67}Si_{0.84}$.

Figure 3(b) compares the experimental μ_s with the theoretical m_{spin} for series-A CMFS films with various values of β' in $Co_2Mn_{0.73}Fe_{\beta'}Si_{0.84}$. Good agreement between μ_s and m_{spin} was obtained for the entire δ range from $\delta = 0.73$ ($\beta' = 0$) to 1.40 ($\beta' = 0.67$). Note that the μ_s value of $\delta = 1.40$ ($\beta' = 0.67$) was apparently lower than its Z_t–24, but it was well reproduced by the m_{spin} value. The overall agreement indicates that the proposed antisite-based SSFU compositions properly describe the SSFU compositions of off-stoichiometric quaternary CMFS of series A.

Figure 3(c) shows the δ dependence of the TMR ratio at 4.2 K of CMFS MTJs having the corresponding series-A films as the lower and upper electrodes, as previously reported in Ref. 47. We found a clear correspondence between the δ dependence of the TMR ratio at 4.2 K with that of the experimental μ_s. More specifically, MTJs that had CMFS films whose experimental μ_s got closer to the half-metallic Z_t–24 value exhibited higher TMR ratios at 4.2 K. A similar film composition dependence of the TMR ratio was observed at RT.

Now let us discuss the origin of the film composition dependences of μ_s of series-A CMFS films and the TMR ratio of series-A CMFS MTJs. Figures 4(a)-(d) show the local density of states (LDOS) for Mn at its ordinary site ($Mn_{Mn/Fe}$), Fe at its ordinary site ($Fe_{Mn/Fe}$), Co at its ordinary site (Co_{Co}), and Co at the nominal Mn/Fe site (antisite $Co_{Mn/Fe}$) for series-A CMFS. Here, the LDOS of $Mn_{Mn/Fe}$ features a wide half-metal gap for the minority-spin states around E_F over the entire range of β' investigated (from $\beta' = 0$ ($\delta = 0.73$) to 0.67 ($\delta = 1.40$)), while the LDOS of $Fe_{Mn/Fe}$ shows a finite density for the minority-spin states at E_F over the entire range. In contrast, the LDOS of antisite $Co_{Mn/Fe}$ for δ-deficient CMFS with $\delta = 0.86$ ($\beta' = 0.13$) and 1.0 ($\beta' = 0.27$) had a peak in the minority-spin DOS around E_F with an appreciable density of states similar to that of Mn-deficient CMS [31] (corresponding to $\beta' = 0$ ($\delta = 0.73$) in the plot). (The critical δ value for which the $Co_{Mn/Fe}$ antisite disappears (δ_c) from the nominal SSFU composition of $Co_2Mn_{\alpha'}Fe_{\beta'}Si_\beta$ is given by $\delta_c = 2-\beta = 1.16$ for $\beta = 0.84$. Thus, the nominal SSFU compositions for $\delta = 1.30$ ($\beta' = 0.57$) and $\delta = 1.40$ ($\beta' = 0.67$) do not contain $Co_{Mn/Fe}$ antisites. In addition, the LDOS curve of Co at the ordinary site (Co_{Co}) for δ-deficient, $\delta = 0.86$ ($\beta' = 0.13$) CMFS had a peak in the minority-spin DOS around E_F (as did Mn-deficient, $\beta' = 0.0$ ($\delta = 0.73$) CMS), although the height was much smaller than that for $Co_{Mn/Fe}$. This result suggests that $Co_{Mn/Fe}$ antisites in (Mn+Fe)-deficient CMFS also affect the electronic state of Co atoms at the ordinary sites in a similar way as in Mn-deficient CMS [31]. Figure 5(a) plots the total DOS of series-A CMFS ($Co_2Mn_{0.73}Fe_{\beta'}Si_{0.84}$) for various β', while Fig. 5(b) plots those of δ-rich series-B CMFS ($Co_2Mn_{\alpha'}Fe_{\beta'}Si_{0.84}$ with $\delta = \alpha'+\beta' = 1.40$) with varying α' and β'. The total DOS curve of δ-deficient, $\delta = 0.86$ ($\beta' = 0.13$) CMFS showed a characteristic peaked structure around E_F in the half-metal gap, with an appreciable DOS at the peak, like that of Mn-deficient, $\beta' = 0$ ($\delta = 0.73$) CMS. This peak also occurred for the $\delta = 1.0$ ($\beta' = 0.27$) CMFS although the height was significantly lower. This lowering of the height is due to the reduced $Co_{Mn/Fe}$ ratio in the SSFU composition of $\delta = 1.0$ ($\beta' = 0.27$) CMFS (Table I) described above. On the other hand, although the peak in the total DOS curve disappeared, a small minority-spin DOS remained around E_F in the half-metal gap for δ-rich,

$\delta = 1.30$ ($\beta' = 0.57$) and $\delta = 1.40$ ($\beta' = 0.67$) CMFS. The disappearance of the peak in the minority-spin DOS corresponds to the disappearance of Co at the nominal Mn/Fe site in their nominal SSFU compositions. Thus, the apparently lower μ_s value than its Z_t-24 for $\delta = 0.73$ ($\beta' = 0$) is due to the deviation of the electronic state from half-metallicity caused by the minority-spin DOS around E_F, as discussed previously [31]. On the other hand, that μ_s is closer but slightly lower than its Z_t-24 value for $\delta = 1.0$ ($\beta' = 0.27$) CMFS is consistent with an electronic state improved in terms of half-metallicity as evidenced by the lowering of the peak of the minority-spin in-gap states around E_F.

We theoretically calculated the δ dependence of the spin magnetic moments of Co, Mn, and Fe atoms at their respective ordinary site and antisite for series-A CMFS by using the KKR-CPA method. Figure 6 shows the calculated spin magnetic moments of Mn, Fe, and Co at the nominal Mn/Fe sites, $m_{spin}(Mn_{Mn/Fe})$, $m_{spin}(Fe_{Mn/Fe})$, and $m_{spin}(Co_{Mn/Fe})$. m_{spin} for antisite Co at the nominal Mn/Fe site is much smaller than those for Mn and Fe ($m_{spin}(Co_{Mn/Fe}) = 1.77\mu_B$ versus $m_{spin}(Mn_{Mn/Fe}) = 3.15\mu_B$, and $m_{spin}(Fe_{Mn/Fe}) = 2.93\mu_B$ for series-A CMFS with $\delta = 1.0$ ($\beta' = 0.27$)). This result supports the conclusion that the origin of the slightly lower μ_s than Z_t-24 for δ-deficient, $\delta = 1.0$ ($\beta' = 0.27$) CMFS is the existence of $Co_{Mn/Fe}$ antisites. Compared with the μ_s of δ-deficient, $\delta = 1.0$ ($\beta' = 0.27$) CMFS, the μ_s of δ-rich, $\delta = 1.30$ ($\beta' = 0.57$) CMFS is close to its Z_t-24 value. This behavior is consistent with the disappearance of Co_{Mn} antisites in the nominal SSFU composition.

Next, let us discuss the origin of the lower μ_s than the half-metallic Z_t-24 value for heavily Fe-doped $\delta = 1.40$ ($\beta' = 0.67$). By comparing the total DOS curve of $\delta = 1.40$ ($\beta' = 0.67$) CMFS with that of Mn-rich, lightly Fe-doped $\alpha' = 1.24$ ($\beta' = 0.16$) CMFS (Fig. 5(b)) (note that $\delta = 1.40$ ($\beta' = 0.67$) CMFS belongs to not only series-A but also series-B), we found that $\delta = 1.40$ ($\beta' = 0.67$) CMFS featured a narrower half-metal gap region with rounded falling and rising edges of the minority-spin DOS at the top of the valence band and the bottom of the conduction band for minority spins. Furthermore, $\delta = 1.40$ ($\beta' = 0.67$) had a finite DOS at E_F in the half-metal gap region. These features are due to the increased Fe atomic ratio (ξ) in the nominal Mn/Fe site in the type III SSFU composition for δ-rich CMFS, where ξ is determined as $\xi = \beta'/(\alpha'+\beta')$, and thus they were observed for $\delta = 1.30$ ($\beta' = 0.57$) and $\delta = 1.40$ ($\beta' = 0.67$) series-A CMFS that had relatively high ξ values ranging from 0.44 to 0.48. To be precise, the structure featuring a narrow half-metal gap region and a finite minority-spin DOS at E_F for the $\delta = 1.30$ ($\beta' = 0.57$) and $\delta = 1.40$ ($\beta' = 0.67$) CMFS should be called a quasi-half-metal gap. The finite minority-spin DOS at E_F in the quasi-half-metal gap for $\delta = 1.30$ ($\beta' = 0.57$) and $\delta = 1.40$ ($\beta' = 0.67$) is due to the finite LDOS of Fe at its ordinary site (Fig. 4(b)). The origin of the decrease in μ_s from its Z_t-24 value for heavily Fe-doped $\delta = 1.40$ ($\beta' = 0.67$) is the smaller local m_{spin} of ordinary-site Fe than that of ordinary-site Mn (Fig. 6) and the larger ξ of up to 0.48 for heavily Fe-doped $\delta = 1.40$ ($\beta' = 0.67$).

Now let us discuss the origin of the δ dependence of the TMR ratio at 4.2 K of series-A CMFS MTJs with $Co_2Mn_{0.73}Fe_{\beta'}Si_{0.84}$ in comparison with the results of the KKR-CPA calculations. To do this, we semi-quantitatively compared the experimentally deduced tunneling spin polarizations, P_{exp}, with the theoretical spin polarizations. We did so because a straightforward first-principles calculation of the TMR ratio for epitaxial MTJs with electrodes with off-stoichiometric compositions is not realistic because of the lack of

translational symmetry in the electrodes. We compared P_{exp} with $P_{th}(sp)$ determined by considering only the contributions from s-, and p-orbital components to the majority- and minority-spin DOS at E_F, $D_M(sp)$ and $D_m(sp)$, respectively, for series-A CMFS electrodes. $P_{th}(sp)$ is defined as

$$P_{th}(sp) = \frac{D_M(sp) - D_m(sp)}{D_M(sp) + D_m(sp)}. \qquad (1)$$

We also made a comparison between P_{exp} and the theoretical spin polarization $P_{th}(spd)$, which takes into consideration all the contributions from s-, p- and d-orbital components to the majority- and minority-spin DOS, $D_M(spd)$ and $D_m(spd)$. $P_{th}(spd)$ is defined as

$$P_{th}(spd) = \frac{D_M(spd) - D_m(spd)}{D_M(spd) + D_m(spd)}. \qquad (2)$$

We estimated the tunneling spin polarization, P_{exp}, which is involved in electron tunneling in MTJs, from the TMR ratio at a low temperature, 4.2 K, by using the Julliere model [56] with a modified interpretation from the original one, as described below. The original Julliere model was derived by assuming that the tunneling matrix element for tunneling from the state characterized by a crystal momentum k to k' at E_F is independent of k and k' and is constant for any tunneling process from k to k'. As a result, the original model takes into account all the majority- and minority-spin density of states at E_F in the spin polarization P. However, the tunneling probability from k to k' is strongly dependent on the wave function symmetry in epitaxial, single-crystalline MTJs [57,58]. Accordingly, in epitaxial MgO-based MTJs, including CMS/MgO-based MTJs [59], where the transverse crystal momentum of an electron is conserved for tunneling, an electron with a Δ_1-symmetry wave function at E_F has a higher transmission probability. To make a semi-quantitative comparison, we assumed that only the electronic states of the majority- and minority-spin bands at E_F that satisfy the condition of coherent tunneling contribute to tunneling in CMS/MgO- and CMFS/MgO-based MTJs at 4.2 K. Furthermore, we assumed that all these electronic states have an equal transmission probability. These assumption lead to the same expression for the TMR ratio as the Julliere model, i.e.,

$$TMR = \frac{2P_{exp}^2}{1 - P_{exp}^2}, \qquad (3)$$

where the tunneling spin polarization P_{exp} corresponds to a spin polarization determined by the majority- and minority-spin DOS at E_F effectively contributing to coherent tunneling. Here, we assumed that the lower and upper electrodes had an identical tunneling spin polarization.

The experimental dependence of P_{exp} on δ for series-A CMFS with $Co_2Mn_{0.73}Fe_{\beta'}Si_{0.84}$ electrodes are compared with those of $P_{th}(sp)$ and $P_{th}(spd)$ in Fig. 7. The P_{exp} values, that increased with increasing δ from $\delta = 0.73$ ($\beta' = 0$) to $\delta = 1.35$ ($\beta' = 0.62$) were semi-quantitatively well explained by the $P_{th}(sp)$ values. Note that these CMFS electrodes

11

showed higher P_{exp} values, typically P_{exp} = 0.946 for δ = 1.35 (β' = 0.62), than the Mn-deficient CMS electrode with δ = 0.73 (β' = 0), which showed a lower P_{exp} of 0.87. In more detail, P_{exp} significantly increased from δ = 0.73 (β' = 0) to δ = 1.24 (β' = 0.51). After that, it slightly increased, reaching a maximum at δ = 1.35 (β' = 0.62), and then decreased upon a further increase in δ to δ = 1.40 (β' = 0.67). This experimental behavior was well reproduced by $P_{th}(sp)$, although there was a slight difference in the δ value that gave the highest P value; i.e., $P_{th}(sp)$ increased from δ = 0.73 (β' = 0) to δ = 1.24 (β' = 0.51), after which it gradually decreased upon a further increase in δ to δ = 1.40 (β' = 0.67). The significant increase in P_{exp} from δ = 0.73 (β' = 0) to δ = 1.24 (β' = 0.51) is due to the decrease in $Co_{Mn/Fe}$ antisites in the SSFU composition with increasing δ in going from a (Mn+Fe)-deficient composition to a (Mn+Fe)-rich one. On the other hand, the decrease in P_{exp} from δ = 1.35 (β' = 0.62) to δ = 1.40 (β' = 0.67) is due to the influence of the increasing Fe/(Mn+Fe) atomic ratio on the half-metallicity via the spin-resolved electronic state. This slight difference in the dependence of P_{exp} and $P_{th}(sp)$ on δ is ascribed to the following reasons: first, there remained a small amount of residual $Co_{Mn/Fe}$ antisites in the actual SSFU composition for CMFS that had the nominally $Co_{Mn/Fe}$ antisite-free type III SSFU composition, and the residual $Co_{Mn/Fe}$ antisites were further suppressed with a (Mn+Fe)-rich composition, as will be discussed in Sec. III B. Second, the increased Fe/(Mn+Fe) atomic ratio degraded the half-metallicity, as discussed above. Thus, there should be a competition between these two effects that results in a slight difference in the dependences of P_{exp} and $P_{th}(sp)$ on δ.

On the other hand, the P_{exp} values for various δ were significantly different from $P_{th}(spd)$. For the negative $P_{th}(spd)$ of δ = 0.73 (β' = 0), its absolute value should be compared with P_{exp}; but this comparison still results in a big difference between P_{exp} and the absolute value of $P_{th}(spd)$ for δ = 0.73 (β' = 0). A comparison of P_{exp} with $P_{th}(sp)$ and $P_{th}(spd)$ for series-A CMFS indicates that the tunneling spin polarization, which is responsible for tunneling in CMFS MTJs in which coherent tunneling is dominant, is mainly explained by $P_{th}(sp)$. This finding is in agreement with the previous findings for CMS MTJs [31].

In summary, the dependences of μ_s of series-A CMFS films and the TMR ratio at 4.2 K of series-A CMFS MTJs on δ could be consistently explained by the effect of the film composition on the half metallicity. Analyses of the experimental μ_s and the TMR ratios together with first-principles calculations for off-stoichiometric CMFS clarified that $Co_{Mn/Fe}$ antisites in quaternary CMFS are detrimental to half-metallicity, in a similar way as they are in ternary CMS. It was also found that (Mn+Fe)-rich compositions in CMFS led to higher TMR ratios through suppression of harmful $Co_{Mn/Fe}$ antisites. Furthermore, it was indicated that the Fe/(Mn+Fe) ratio influenced the half-metallicity, in particular for the relatively large Fe/(Mn+Fe) ratio. The latter effect is further investigated in Sec. III B for series-B CMFS.

B. Origin of the giant TMR ratio of CMFS MTJs with Mn-rich, lightly Fe-doped CMFS electrodes

In this section, we will discuss how the half-metallicity of (Mn+Fe)-rich CMFS depends on the Fe composition. Then, we will discuss the origin of the giant TMR ratio of CMFS MTJs with Mn-rich, lightly Fe-doped CMFS electrodes. We investigated μ_s for series-B

CMFS, i.e., (Mn+Fe)-rich $Co_2Mn_{\alpha'}Fe_{\beta'}Si_{0.84}$ having a fixed $\delta = \alpha'+\beta' = 1.40$ with various combinations of α' and β' ranging from $\beta' = 0$ ($\alpha' = 1.40$) to $\beta' = 0.67$ ($\alpha' = 0.73$) [Table II]. Furthermore, we experimentally investigated the TMR ratios of CMFS MTJs with Mn-rich, lightly Fe-doped CMFS electrodes as a function of α' in $Co_2Mn_{\alpha'}Fe_{0.16}Si_{0.84}$ (series-C CMFS) for an α'-rich range from $\alpha' = 1.14$ to 1.24 and compared the results with those of the previously reported CMFS MTJs with series-A and series-B CMFS electrodes [47].

Figure 8(a) compares μ_s at 10 K with Z_t-24 and m_{spin} obtained by the KKR-CPA calculations for series-B CMFS films with β' ranging from $\beta' = 0$ ($\alpha' = 1.40$) to $\beta' = 0.67$ ($\alpha' = 0.73$). ($\beta' = 0.67$ ($\alpha' = 0.73$) belongs to both series-A and series-B as noted above.) It was found that the μ_s of $\beta' = 0.16$ ($\alpha' = 1.24$), i.e., $Co_2Mn_{1.24}Fe_{0.16}Si_{0.84}$, in which a small amount of Mn was replaced with Fe in $Co_2Mn_{1.40}Si_{0.84}$, was close to its Z_t-24 value. Similarly, μ_s of β' = 0.40 ($\alpha' = 1.0$) was close to its Z_t-24 value. Thus, the good agreement between μ_s and Z_t-24 for these Heusler alloys indicates that their electronic states are close to being half-metallic in terms of μ_s. Furthermore, their μ_s values were close to the theoretical m_{spin} values. On the other hand, the experimental μ_s for $\beta' = 0$ ($\alpha' = 1.40$), i.e., Mn-rich $Co_2Mn_{1.40}Si_{0.84}$, was evidently lower than its Z_t-24 value, while its theoretical m_{spin} value was in rather good agreement with Z_t-24. Similarly, as mentioned in section III A, μ_s of the heavily Fe-doped β' = 0.67 ($\alpha' = 0.73$) was significantly lower than its Z_t-24 value, while m_{spin} reproduced the experimental μ_s. The origin of this behavior has already been discussed in Sec. III A.

Figure 8(b) shows the TMR ratios at 4.2 K of CMFS MTJs having series-B CMFS films as the lower and upper electrodes as a function of β' (as previously reported in Ref. 47), along with Z_t-24 values on the top axis. Two characteristic results can be seen. Firstly, the TMR ratio significantly increases from $\beta' = 0$ ($\alpha' = 1.40$) to $\beta' = 0.16$ ($\alpha' = 1.24$) (region-a). Indeed, it increases from 1670% at 4.2 K (336% at 290 K) for $\beta' = 0$ ($\alpha' = 1.40$), i.e, $Co_2Mn_{1.40}Si_{0.84}$ to 2610% at 4.2 K (429% at 290 K) for $\beta' = 0.16$ ($\alpha' = 1.24$), i.e., Mn-rich, lightly Fe-doped $Co_2Mn_{1.24}Fe_{0.16}Si_{0.84}$. Thus, this significant increase in the TMR ratio of $\beta' = 0.16$ ($\alpha' = 1.24$) compared with that of $\beta' = 0$ ($\alpha' = 1.40$) coincides with the recovery of μ_s to a value close to the half-metallic Z_t-24 for $\beta' = 0.16$ ($\alpha' = 1.24$). This result is a key to understanding the origin of the giant TMR ratio of the MTJs with Mn-rich, lightly Fe-doped CMFS electrodes. Secondly, the TMR ratio at 4.2 K of the MTJs with series-B films gradually decreases from β' = 0.16 ($\alpha' = 1.24$) to $\beta' = 0.67$ ($\alpha' = 0.73$) (region-b). Indeed, it gradually decreases from 2610% at 4.2 K (429% at 290 K) for Mn-rich, lightly Fe-doped $\beta' = 0.16$ ($\alpha' = 1.24$) to 1290% at 4.2 K (304% at 290 K) for heavily Fe-doped $\beta' = 0.67$ ($\alpha' = 0.73$). The drop in the TMR ratio for $\beta' = 0.67$ ($\alpha' = 0.73$) corresponds to a lower μ_s than its Z_t-24.

Figure 5(b) shows the spin-resolved total DOS curves of series-B CMFS with various β' values. The KKR-CPA calculations predicted that Mn-rich, lightly Fe-doped CMFS, i.e., α' = 1.24 ($\beta' = 0.16$), retains a distinct half-metallic gap structure characterized by sharp falling and rising edges of the minority-spin DOS at the top of the valence band and the bottom of the conduction band, although the minority-spin DOS in the half-metal gap region slightly increased with increasing energy across E_F, resulting in a small finite minority-spin DOS at E_F. On the other hand, the KKR-CPA calculations for $Co_2Mn_{1.40}Si_{0.84}$ ($\alpha' = 1.40$, $\beta' = 0$) based on the Co_{Mn}-antisite-free SSFU composition (Table II) indicated a more complete half-metallic structure, as has been predicted for Mn-rich CMS with type III SSFU composition [31,50].

13

The theoretically predicted half-metallic character of $\alpha' = 1.24$ ($\beta' = 0.16$) CMFS is consistent with the experimentally observed giant TMR ratio and the μ_s being close to its Z_t-24 value. The minority-spin DOS at E_F gradually increased when β' was further increased from $\beta' = 0.16$ ($\xi = 0.11$) to $\beta' = 0.67$ ($\xi = 0.48$) in region-b, as shown in Fig. 5(b). This is due to the more rounded rising edge at the bottom of the minority-spin conduction band for CMFS with increased ξ, and its origin can be mainly ascribed to the LDOS curve of Fe at the ordinary Mn/Fe site (not shown).

To compare the experimentally obtained TMR ratios for various β' values with the theoretically derived spin polarizations for series-B CMFS, we plot P_{exp} along with $P_{th}(sp)$ and $P_{th}(spd)$ as a function of β' in Fig. 9, where the P_{exp} values are estimated from the TMR ratios at 4.2 K using the Julliere model with the modified interpretation in Sec. III A. The figure shows that P_{exp} for the entire β' range from $\beta' = 0$ ($\alpha' = 1.40$) to $\beta' = 0.67$ ($\alpha' = 0.73$) is generally in good agreement with $P_{th}(sp)$ as in the case of series-A CMFS. In contrast, the difference between P_{exp} and $P_{th}(spd)$ is significant; in particular, the degree of the difference increases as P_{exp} decreases. Summarizing the comparison of P_{exp} with $P_{th}(sp)$ and $P_{th}(spd)$ for series-A and series-B CMFS, we find that P_{exp} for highly spin-polarized CMFS electrodes is semi-quantitatively in agreement with $P_{th}(sp)$ but not $P_{th}(spd)$. This finding is reasonable because tunneling in epitaxial MgO-based MTJs is dominated by coherent tunneling of electrons of Δ_1 symmetry states of CMFS in which itinerant s- and $p(z)$ states rather than $d(3z^2-r^2)$ states are the main components. Note that the agreement between P_{exp} and $P_{th}(sp)$ was better for electrodes with higher P_{exp}.

Next, let us compare the β' dependence of P_{exp} with that of $P_{th}(sp)$ in more detail, in particular for a lightly Fe-doped composition range (region-a). The high P_{exp} of 0.964 corresponding to a giant TMR ratio of 2610% at 4.2 K for $\alpha' = 1.24$ ($\beta' = 0.16$) CMFS was close to the $P_{th}(sp)$ of 0.984. This high level of agreement is due to the theoretically predicted half-metal gap. In contrast, the lower P_{exp} of 0.945 (the TMR ratio of 1670% at 4.2 K) for $Co_2Mn_{1.40}Si_{0.84}$ ($\alpha' = 1.40$, $\beta' = 0$) was in apparent disagreement with that of the theoretically predicted spin polarization of almost 100%. Indeed, the KKR-CPA calculations predicted $P_{th}(sp) = 0.995$ and $P_{th}(spd) = 0.991$, due to the more complete half-metal gap for ($\alpha' = 1.40$, $\beta' = 0$). Summarizing the experimental results on μ_s and the TMR ratio, we conclude that although the electronic state of Mn-over-rich CMS with $\alpha > \alpha_c$ ($Co_2Mn_{1.40}Si_{0.84}$ having $\alpha = 1.40$) slightly deviated from the theoretically predicted half-metallic Slater-Pauling value of Z_t-24, the Mn-rich, lightly Fe-doped CMFS with $\delta > \alpha_c$ ($Co_2Mn_{1.24}Fe_{0.16}Si_{0.84}$ having $\delta = 1.40$) still retained the half-metallic state. Here α_c is the critical Mn-composition over which the TMR ratio of CMS/MgO/CMS MTJs showed a decrease. We have supposed that the origin of the inconsistency between the experimental and theoretical results for Mn-over-rich CMS with $\alpha > \alpha_c$ is the slight deviation of the SSFU composition from the predicted Co_{Mn}-antisite-free SSFU composition for CMS with $\alpha > \alpha_c$ and that the actual SSFU composition for CMS with $\alpha > \alpha_c$ had a certain amount of Co_{Mn} antisites that reappeared [31]. The lower μ_s than Z_t-24 and the decreased TMR ratio for $Co_2Mn_{1.40}Si_{0.84}$ can be explained by this supposition. The origin of this deviation has been assumed to be the appearance of a second phase such as antiferromagnetic Mn_3Si with a Neel temperature of 25 K [31,55], although it has not been experimentally confirmed. The experimentally demonstrated

14

half-metallic character of Mn-rich, lightly Fe-doped CMFS indicates the suppression of the deviation of the SSFU composition from the proposed Co_{Mn}-antisite-free SSFU composition for Mn-rich CMS even with $\alpha > \alpha_c$ by replacing a small amount of Mn by Fe. Thus, the significant increase in the TMR ratio with increasing β' in a small β' range from $\beta' = 0$ ($\alpha' = 1.40$) to $\beta' = 0.16$ ($\alpha' = 1.24$) in the series-B CMFS MTJs (Fig. 8(b)) can be explained by the recovery of the half-metallic electronic state via the recovery of the $Co_{Mn/Fe}$-antisite-free type III SSFU composition induced by replacing a small amount of Mn with Fe. However, this idea is not sufficient to explain why the $\alpha' = 1.24$ ($\beta' = 0.16$) CMFS MTJ had a significantly higher TMR ratio than the highest TMR ratio that the Mn-rich CMS MTJs exhibited [9,47].

To further clarify the origin of the giant TMR ratio for Mn-rich, lightly Fe-doped CMFS, we adopted a more systematic approach to lightly Fe-doped CMFS MTJs and investigated the dependence of their TMR ratio on the film composition. In this approach, we investigated CMFS MTJs with lightly Fe-doped CMFS electrodes by systematically increasing α' with a fixed $\beta' = 0.16$. Figures 10(a) and (b) show the TMR ratios at 4.2 K and 290 K of CMFS MTJs with lightly Fe-doped ($\beta' = 0.16$), Mn-rich $Co_2Mn_{\alpha'}Fe_{0.16}Si_{0.84}$ electrodes (series-C CMFS) as a function of α' ranging from $\alpha' = 1.14$ ($\delta = 1.30$) to 1.24 ($\delta = 1.40$). For the sake of comparison, the figures also show the TMR ratios at 4.2 K and 290 K of identically prepared CoFe-buffered CMS MTJs having $Co_2Mn_{\alpha}Si_{0.84}$ electrodes as a function of α ranging from 0.73 to 1.40 [47]. The TMR ratio of CMS MTJs increased with α to 2110% at 4.2 K and 370% at 290 K for $\alpha = 1.30$; beyond $\alpha_c \sim 1.33$, i.e., the critical Mn composition in the CMS series of $Co_2Mn_{\alpha}Si_{0.84}$, it decreased to 1670% at 4.2 K and 336% at 290 K for $\alpha = 1.40$. Note that the TMR ratios of the $\delta = 1.30$ ($\beta' = 0.16$) CMFS MTJ (2110% at 4.2 K and 366% at 290 K) were almost equal to those obtained for the $\alpha = 1.30$ CMS MTJ. Most importantly, we found an increase in the TMR ratio for CMFS MTJs with lightly Fe-doped $Co_2Mn_{\alpha'}Fe_{0.16}Si_{0.84}$ when δ was increased beyond 1.30 up to $\delta = 1.40$. This resulted in significantly high TMR ratios of 2610% at 4.2 K and 429% at 290 K for the CMFS MTJ with $\alpha' = 1.24$ and $\beta' = 0.16$ ($\delta = 1.40$). This dependence was in sharp contrast to the decrease in the TMR ratio for CMS MTJs when α was larger than α_c.

Note that the increase in the TMR ratio with α' in the series-C lightly Fe-doped CMFS is on the extended line of the increase in the TMR ratio for CMS MTJs (Fig. 10). The increase in the TMR ratio with increasing α for CMS MTJs with $Co_2Mn_{\alpha}Si_{\beta}$ (β is about 1.0) has been explained by a decrease in Co_{Mn} antisites with increasing α in the Mn-deficient composition region ($\alpha < 2-\beta$) and by a further suppression of residual Co_{Mn} antisites in the nominally Co_{Mn}-antisite-free type III SSFU composition ($\alpha > 2-\beta$) by further increasing α [8,31]. The $\alpha = 1.24$ and $\alpha = 1.30$ CMS electrodes featured the Co_{Mn}-antisite-free type III SSFU compositions. The first-principles calculations have predicted almost 100% spin polarization for such CMS featuring the Co_{Mn}-antisites-free type III SSFU composition [31,35]. Indeed, the KKR-CPA calculations predicted $P_{th}(sp)$ values of about 0.995 and $P_{th}(spd)$ of about 0.991 for these CMS electrodes [31]. The total DOS curves of series-C CMFS ($\alpha' = 1.14$, 1.19, and 1.24); one of which for $\alpha' = 1.24$ ($\delta = 1.40$) is shown in Fig. 5(b), are almost identical for the entire α' range from $\alpha' = 1.14$ ($\delta = 1.30$) to $\alpha' = 1.24$ ($\delta = 1.40$) and commonly show a distinct half-metal gap as described above for $\delta = 1.40$ ($\alpha' = 1.24$). These half-metal gap structures led to the $P_{th}(sp)$ values being close to the half-metallic value and almost constant for series-C

15

CMFS, ranging from 0.984 for δ = 1.30 (α' = 1.14) to 0.987 for δ = 1.40 (α' = 1.24). Thus, the experimentally observed increase in the TMR ratio of CMS MTJs from α = 1.24 (TMR ratio of 1790% at 4.2 K, corresponding to P_{exp} = 0.948) to α = 1.30 (TMR ratio of 2110%, P_{exp} = 0.956) and the continuous increase in the TMR ratio of series-C CMFS from δ = 1.30 (TMR ratio of 2110%, P_{exp} = 0.956) to δ = 1.40 (TMR ratio of 2610%, P_{exp} = 0.964) can't be explained by the almost constant half-metallic $P_{th}(sp)$ values derived from the KKR-CPA calculations based on the nominal SSFU compositions for CMS with α ranging from 1.24 to 1.30 and for series-C CMFS. The observed increase in the TMR ratio should be explained by another factor that is not included in the SSFU compositions. The enhanced TMR ratio obtained by increasing α for CMS and by increasing δ in lightly Fe-doped CMFS suggests an identical origin, i.e., the suppression of residual Co antisites at the nominal Mn site in CMS or the nominal Mn/Fe site in CMFS by increasing the Mn ratio with respect to Co in the nominal type III SSFU compositions. This idea is the same as that for Mn-rich CMS [5,31,55]. Note that the residual Co_{Mn} antisite for CMS or lightly Fe-doped CMFS is not taken into account in the type III, Co_{Mn}-antisite-free SSFU composition model. However, the further increase in the TMR ratio for the Mn-rich composition in CMS and lightly Fe-doped CMFS suggests that detrimental Co_{Mn} antisites are hard to avoid in experimentally prepared films even with a stoichiometric composition or Mn-rich composition, but that they can be reduced by enriching the compositions with more Mn. However, there is a certain critical Mn composition for CMS [5,31]. This study indicated that the critical Mn composition for CMS became larger as a result of replacing a small amount of Mn by Fe. Accordingly, a further reduction in the residual Co_{Mn}-antisites occurred as a result of δ being larger in CMFS than in Mn-rich CMS with α up to α_c. Thus, we conclude that enhanced half-metallicity due to further reduction of residual $Co_{Mn/Fe}$ antisites is the origin of the giant TMR ratio of CMFS MTJs with Mn-rich, lightly Fe-doped CMFS electrodes.

Finally, let us discuss the origin of the gradual decrease in the TMR ratio with increasing β' for series-B CMFS in region-b. The P_{exp} values derived by the TMR ratios at 4.2 K for region-b ranging from β' = 0.16 (α' = 1.24) to β' = 0.67 (α' = 0.73) were in good agreement with $P_{th}(sp)$ obtained from the KKR-CPA calculations. The gradual decrease in P_{exp} with increasing Fe/(Mn+Fe) atomic ratio, ξ, in this region was well reproduced by the first-principles calculations. P_{exp} gradually decreased with increasing β' from P_{exp} = 0.964 (TMR ratio at 4.2 K = 2610%) for β' = 0.16 (α' = 1.24, corresponding to ξ = 0.11) to P_{exp} = 0.931 (TMR ratio at 4.2 K = 1290%) for β' = 0.67 (α' = 0.73, corresponding to ξ = 0.48). The total DOS curves showed that the most enhanced half-metallic electronic state among CMFS of region-b is for lightly Fe-doped β' = 0.16 (α' = 1.24). The minority-spin DOS at E_F gradually increased with increasing ξ. This is due to the more rounded rising edge of the minority-spin DOS at the bottom of the conduction band with increasing ξ and the E_F position crossing this rounded rising edge region. This resulted in the narrower half-metal gap for β' = 0.67 (α' = 0.73) having the highest ξ = 0.48 among series-B CMFS. Furthermore, the majority-spin DOS at E_F gradually decreased with increasing ξ. These factors led to the gradual decrease in $P_{th}(sp)$ with increasing ξ.

IV. CONCLUSION

We investigated how the film compositions in terms of off-stoichiometry and Fe/(Mn+Fe) atomic ratios affect the half-metallicity of the quaternary Heusler alloy $Co_2(Mn,Fe)Si$ (CMFS) by analyzing the saturation magnetization per formula unit, μ_s, of CMFS thin films with various Mn and Fe compositions, the TMR ratios of CMFS/MgO/CMFS MTJs (CMFS MTJs), and first-principles calculations. We also investigated the origin of the giant TMR ratio of up to 2610% at 4.2 K (429% at 290 K) that was recently reported for CMFS MTJs with Mn-rich, lightly Fe-doped CMFS electrodes. The lower μ_s than half-metallic Z_t-24 for (Mn+Fe)-deficient CMFS films was explained by the spin magnetic moment of Co at the nominal Mn/Fe site ($Co_{Mn/Fe}$) being smaller than those of Mn and Fe at their nominal Mn/Fe site. Furthermore, the film composition dependence of the TMR ratio was well explained by the theoretical spin polarizations derived from only the s- and p-orbital components of the DOS at E_F. The experimentally investigated μ_s and TMR ratios in combination with first-principles calculations indicated that $Co_{Mn/Fe}$ antisites in the quaternary alloy are detrimental to half-metallicity, in a similar way as in ternary alloy CMS. It was demonstrated that (Mn+Fe)-rich compositions are highly effective at suppressing harmful $Co_{Mn/Fe}$ antisites and that a relatively small Fe ratio in the total (Mn+Fe) composition retains a half-metallic state. Finally, it was revealed that residual $Co_{Mn/Fe}$ antisites were further suppressed in lightly Fe-doped CMFS because the available (Mn+Fe) composition in (Mn+Fe)-rich CMFS became larger than the critical Mn composition in Mn-rich CMS. This resulted in a giant TMR ratio for CMFS MTJs with Mn-rich, lightly Fe-doped CMFS electrodes. Our findings indicate that appropriate control of off-stoichiometry and the film composition of quaternary Heusler alloy CMFS toward a Mn-rich, lightly Fe-doped composition is highly promising for fully utilizing the half-metallicity of quaternary CMFS thin films as spin source materials.

References

[1]   I. Žutić, J. Fabian, and S. Das Sarma, Rev. Mod. Phys. **76**, 323 (2004).

[2]   S. A. Wolf, D. D. Awschalom, R. A. Buhrman, J. M. Daughton, S. von Molnár, M. L. Roukes, A. Y. Chtchelkanova, and D. M Treger, Science **294**, 1488 (2001).

[3]   R. A. de Groot, F. M. Müeller, P. G. vanEngen, and K. H. J. Buschow, Phys. Rev. Lett. **50**, 2024 (1983).

[4]   T. Graf, C. Felser, and S. S. P. Parkin, Prog. Solid State Chem. **39**, 1 (2011).

[5]   M. Yamamoto, T. Marukame, T. Ishikawa, K.-i. Matsuda, T. Uemura, and M. Arita, J. Phys. D: Appl. Phys. **39**, 824 (2006).

[6]   T. Ishikawa, T. Marukame, H. Kijima, K.-i. Matsuda, T. Uemura, M. Arita, and M. Yamamoto, Appl. Phys. Lett. **89**, 192505 (2006).

[7]   N. Tezuka, N. Ikeda, F. Mitsuhashi, and S. Sugimoto, Appl. Phys. Lett. 94, 162504 (2009).

[8]   M. Yamamoto, T. Ishikawa, T. Taira, G.-f. Li, K.-i. Matsuda, and T. Uemura, J. Phys.: Condens. Matter **22**, 164212 (2010).

[9]   H.-x. Liu, Y. Honda, K.-i. Matsuda, M. Arita, T. Uemura, and M. Yamamoto, Jpn. J. Appl. Phys. **51**, 093004 (2012).

[10] H.-x. Liu, Y. Honda, T. Taira, K.-i. Matsuda, M. Arita, T. Uemura, and M. Yamamoto, Appl. Phys. Lett. **101**, 132418 (2012).

[11] T. Marukame, T. Ishikawa, T. Taira, K.-i. Matsuda, T. Uemura, and M. Yamamoto, Phys. Rev. B **81**, 134432 (2010).

[12] W. Wang, E. Liu, M. Kodzuka, H. Sukegawa, M. Wojcik, E. Jedryka, G. H. Wu, K. Inomata, S. Mitani, and K. Hono, Phys. Rev. B **81**, 140402(R) (2010).

[13] T. Furubayashi, K. Kodama, H. Sukegawa, Y. K. Takahashi, K. Inomata, and K. Hono, Appl. Phys. Lett. **93**, 122507 (2008).

[14] Y. Sakuraba, K. Izumi, T. Iwase, S. Bosu, K. Saito, K. Takanashi, Y. Miura, K. Futatsukawa, K. Abe, and M. Shirai, Phys. Rev. B **82**, 094444 (2010).

[15] Y. K. Takahashi, A. Srinivasan, B. Varaprasad, A. Rajanikanth, N. Hase, T. M. Nakatani, S. Kasai, T. Furubayashi, and K. Hono, Appl. Phys. Lett. **98**, 152501 (2011).

[16] M. J. Carey, S. Maat, S. Chandrashekariaih, J. A. Katine, W. Chen, B. York, and J. R. Childress, J. Appl. Phys. 109, 093912 (2011).

[17] J. Sato, M. Oogane, H. Naganuma, and Y. Ando, Appl. Phys. Express **4**, 113005 (2011).

[18] Y. Sakuraba, M. Ueda, Y. Miura, K. Sato, S. Bosu, K. Saito, M. Shirai, T. J. Konno, and K. Takanashi, Appl. Phys. Lett. **101**, 252408 (2012).

[19] X. Y. Dong, C. Adelmann, J. Q. Xie, C. J. Palmstrøm, X. Lou, J. Strand, P. A. Crowell, J.-P. Barnes, and A. K. Petford-Long, Appl. Phys. Lett. **86**, 102107 (2005).

[20] M. Ramsteiner, O. Brandt, T. Flissikowski, H. T. Grahn, M. Hashimoto, J. Herfort, and H. Kostial, Phys. Rev. B **78**, 121303(R) (2008).

[21] T. Akiho, J. Shan, H.-x. Liu, K.-i. Matsuda, M. Yamamoto, and T. Uemura, Phys. Rev. B. **87**, 235205 (2013).

[22] P. Bruski, Y. Manzke, R. Farshchi, O. Brandt, J. Herfort, and M. Ramsteiner, Appl. Phys. Lett. **103**, 052406 (2013).

[23]   T. Saito, N. Tezuka, M. Matsuura, and S. Sugimoto, Appl. Phys. Express **6**, 103006 (2013).

[24]   Y. Ebina, T. Akiho, H.-x. Liu, M. Yamamoto, and T. Uemura, Appl. Phys. Lett. **104**, 172405 (2014).

[25]   T. Uemura, T. Akiho, Y. Ebina, and M. Yamamoto, Phys. Rev. B **91**, 140410(R) (2015).

[26]   S. Ishida, S. Fujii, S. Kashiwagi, and S. Asano, J. Phys. Soc. Jpn. **64**, 2152 (1995).

[27]   S. Picozzi, A. Continenza, and A. J. Freeman, Phys. Rev. B **66**, 094421 (2002).

[28]   I. Galanakis, P. H. Dederichs, and N. Papanikolaou, Phys. Rev. B **66**, 174429 (2002).

[29]   P. J. Webster, J. Phys. Chem. Solids **32**, 1221 (1971).

[30]   S. Picozzi, A. Continenza, and A. J. Freeman, Phys. Rev. B **69**, 094423 (2004).

[31]   G.-f. Li, Y. Honda, H.-x. Liu, K.-i. Matsuda, M. Arita, T. Uemura, M. Yamamoto, Y. Miura, M. Shirai, T. Saito, F. Shi, and P. M. Voyles, Phys. Rev. B **89,** 014428 (2014).

[32]   J.-P. Wüstenberg, R. Fetzer, M. Aeschlimann, M. Cinchetti, J. Minár, Jürgen Braun, H. Ebert, T. Ishikawa, T. Uemura, and M. Yamamoto, Phys. Rev. B **85**, 064407 (2012).

[33]   S. Ouardi, G. H. Fecher, S. Chadov, B. Balke, X. Kozina, C. Felser, T. Taira, and M. Yamamoto, Applied Physics A: Materials Science & Processing **111**, 395 (2013).

[34]   X. Kozina, J. Karel, S. Ouardi, S. Chadov, G. H. Fecher, C. Felser, G. Stryganyuk, B. Balke, T. Ishikawa, T. Uemura, M. Yamamoto, E. Ikenaga, S. Ueda, and K. Kobayashi, Phys. Rev. B **89**, 125116 (2014).

[35]   R. Fetzer, S. Ouardi, Y. Honda, H.-x. Liu, S. Chadov, B. Balke, S. Ueda, M. Suzuki, T. Uemura, M. Yamamoto, M. Aeschlimann, M. Cinchetti, G. H. Fecher, and C. Felser, J. Phys. D: Appl. Phys. **48**, 164002 (2015).

[36]   D. Asakura, T. Koide, S. Yamamoto, K. Tsuchiya, T. Shioya, K. Amemiya, V. R. Singh, T. Kataoka, Y. Yamazaki, Y. Sakamoto, A. Fujimori, T. Taira, and M. Yamamoto, Phys. Rev. B **82**, 184419 (2010).

[37]   V. R. Singh, V. K. Verma, K. Ishigami, G. Shibata, T. Kadono, A. Fujimori, D. Asakura, T. Koide, Y. Miura, M. Shirai, G.-f. Li, T. Taira, and M. Yamamoto, Phys. Rev. B **86**, 144412 (2012).

[38]   V. R. Singh, V. K. Verma, K. Ishigami, G. Shibata, A. Fujimori, T. Koide, Y. Miura, M. Shirai, T. Ishikawa, G. -f. Li, and M. Yamamoto, J. Appl. Phys. **117**, 203901 (2015).

[39]   M. Kallmayer, H. J. Elmers, B. Balke, S. Wurmehl, F. Emmerling, G. H. Fecher, and C. Felser, J. Phys. D: Appl. Phys, **39**, 786 (2006).

[40]   B. Balke, G. H. Fecher, H. C. Kandpal, and C. Felser, K. Kobayashi, E. Ikenaga, J. J. Kim, and S. Ueda, Phys. Rev. B **74**, 104405 (2006).

[41]   G. H. Fecher, B. Balke, S. Ouardi, C. Felser, G. Schönhense, E. Ikenaga, J. J. Kim, S. Ueda, and K. Kobayashi, J. Phys. D: Appl. Phys. **40**, 1576 (2007).

[42]   S. Wurmehl, J. T. Kohlhepp, H. J. M. Swagten, B. Koopmans, M. Wójcik, B. Balke, C. G. F. Blum, V. Ksenofontov, G.H. Fecher, and C. Felser, Appl. Phys. Lett. **91**, 052506 (2007).

[43]   S. Chadov, G. H. Fecher, C. Felser, J. Minár, J. Braun, and H. Ebert, J. Phys. D: Appl. Phys. **42**, 084002 (2009).

[44]   M. Kallmayer, P. Klaer, H. Schneider, E. Arbelo Jorge, C. Herbort, G. Jakob, M. Jourdan, and H. J. Elmers, 2009 Phys. Rev. B **80**, 020406(R) (2009).

[45] M. Oogane, T. Kubota, Y. Kota, S. Mizukami, H. Naganuma, A. Sakuma, and Y. Ando, Appl. Phys. Lett. **96**, 252501 (2010).

[46] T. Kubota, S. Tsunegi, M. Oogane, S. Mizukami, T. Miyazaki, H. Naganuma, and Y. Ando, Appl. Phys. Lett. **94**, 122504 (2009).

[47] H.-x. Liu, T. Kawami, K. Moges, T. Uemura, M. Yamamoto, F. Shi and P. M. Voyles, J. Phys. D: Appl. Phys. **48**, 164001 (2015).

[48] T. Saito, T. Katayama, T. Ishikawa, M. Yamamoto, D. Asakura, and T. Koide, Appl. Phys. Lett. **91**, 262502 (2007).

[49] T. Saito, T. Katayama, T. Ishikawa, M. Yamamoto, D. Asakura, T. Koide, Y. Miura, and M. Shirai, Phys. Rev. B **81**, 144417 (2010).

[50] R. Fetzer, B. Stadtmüller, Y. Ohdaira, H. Naganuma, M. Oogane, Y. Ando, T. Taira, T. Uemura, M. Yamamoto, M. Aeschlimann, and M. Cinchetti, Sci. Rep. **5**, 8537 (2015).

[51] L. G. Parratt, Phys. Rev. **95**, 359 (1954).

[52] W. Kohn and N. Rostoker, Phys. Rev. **94**, 1111 (1954).

[53] H. Akai and P. H. Dederichs, Phys. Rev. B **47**, 8739 (1993).

[54] M. Rasolt and D. J. W. Geldart, Phys. Rev. B **34**, 1325 (1986).

[55] B. Hülsen, M. Scheffler, and P. Kratzer, Phys. Rev. B **79**, 094407 (2009).

[56] M. Jullière, Phys. Lett. **54A**, 225 (1975).

[57] W. H. Butler, X.-G. Zhang, T. C. Schulthess, and J. M. MacLaren, Phys. Rev. B **63**, 054416 (2001).

[58] J. Mathon and A. Umerski, Phys. Rev. B **63**, 220403(R) (2001).

[59] Y. Miura, H. Uchida, Y. Oba, K. Nagao, and M. Shirai, J. Phys.: Condens. Matter **19**, 365228 (2007).

Table I. Empirical formulas, site-specific formula unit (SSFU) composition types, SSFU compositions, measured in-plane (a) and out-of-plane (c) lattice constants, and Z_t-24 values of series-A CMFS films, where Z_t is the valance electron number per formula unit.

$Co_2Mn_\alpha Fe_\beta Si_{0.84}$ ($\alpha' = 0.73$)	SSFU composition type	SSFU composition	a (nm)	c (nm)	Z_t-24
$Co_2Mn_{0.73}Si_{0.84}$	II	$Co_{2.00}[Mn_{0.759}Co_{0.241}][Si_{0.941}Mn_{0.059}]$	0.5610	0.5642	5.658
$Co_2Mn_{0.73}Fe_{0.13}Si_{0.84}$	II	$Co_{2.00}[Mn_{0.711}Fe_{0.127}Co_{0.162}][Si_{0.908}Mn_{0.078}Fe_{0.014}]$			5.741
$Co_2Mn_{0.73}Fe_{0.27}Si_{0.84}$	II	$Co_{2.00}[Mn_{0.669}Fe_{0.248}Co_{0.083}][Si_{0.875}Mn_{0.091}Fe_{0.034}]$	0.5633	0.5673	5.823
$Co_2Mn_{0.73}Fe_{0.51}Si_{0.84}$	III	$[Co_{1.961}Mn_{0.023}Fe_{0.016}][Mn_{0.589}Fe_{0.411}][Si_{0.824}Mn_{0.104}Fe_{0.073}]$			5.951
$Co_2Mn_{0.73}Fe_{0.57}Si_{0.84}$	III	$[Co_{1.932}Mn_{0.038}Fe_{0.030}][Mn_{0.562}Fe_{0.438}][Si_{0.812}Mn_{0.106}Fe_{0.083}]$	0.5643	0.5679	5.981
$Co_2Mn_{0.73}Fe_{0.62}Si_{0.84}$	III	$[Co_{1.909}Mn_{0.049}Fe_{0.042}][Mn_{0.541}Fe_{0.459}][Si_{0.802}Mn_{0.107}Fe_{0.091}]$			6.005
$Co_2Mn_{0.73}Fe_{0.67}Si_{0.84}$	III	$[Co_{1.887}Mn_{0.059}Fe_{0.054}][Mn_{0.521}Fe_{0.479}][Si_{0.792}Mn_{0.108}Fe_{0.099}]$	0.5633	0.5645	6.028

Table II. Empirical formulas, SSFU composition types, SSFU compositions, measured lattice constants a and c, and Z_t-24 values of series-B CMFS films.

$Co_2Mn_\alpha Fe_\beta Si_{0.84}$ ($\delta = \alpha' + \beta' = 1.40$)	SSFU composition type	SSFU composition	a (nm)	c (nm)	Z_t-24
$Co_2Mn_{1.40}Si_{0.84}$	III	$[Co_{1.887}Mn_{0.113}][Mn_{1.00}][Si_{0.792}Mn_{0.208}]$	0.5690	0.5657	5.396
$Co_2Mn_{1.35}Fe_{0.05}Si_{0.84}$	III	$[Co_{1.887}Mn_{0.109}Fe_{0.004}] [Mn_{0.964}Fe_{0.036}][Si_{0.792}Mn_{0.200}Fe_{0.007}]$			5.443
$Co_2Mn_{1.30}Fe_{0.10}Si_{0.84}$	III	$[Co_{1.887}Mn_{0.105}Fe_{0.008}][Mn_{0.029}Fe_{0.071}][Si_{0.792}Mn_{0.193}Fe_{0.015}]$			5.491
$Co_2Mn_{1.24}Fe_{0.16}Si_{0.84}$	III	$[Co_{1.887}Mn_{0.100}Fe_{0.013}][Mn_{0.886}Fe_{0.114}][Si_{0.792}Mn_{0.184}Fe_{0.024}]$	0.5679	0.5666	5.547
$Co_2Mn_{1.16}Fe_{0.24}Si_{0.84}$	III	$[Co_{1.887}Mn_{0.094}Fe_{0.019}][Mn_{0.829}Fe_{0.171}][Si_{0.792}Mn_{0.172}Fe_{0.036}]$			5.623
$Co_2Mn_{1.00}Fe_{0.40}Si_{0.84}$	III	$[Co_{1.887}Mn_{0.081}Fe_{0.032}][Mn_{0.714}Fe_{0.286}][Si_{0.792}Mn_{0.148}Fe_{0.059}]$	0.5656	0.5677	5.774
$Co_2Mn_{0.85}Fe_{0.55}Si_{0.84}$	III	$[Co_{1.887}Mn_{0.069}Fe_{0.044}][Mn_{0.607}Fe_{0.393}][Si_{0.792}Mn_{0.126}Fe_{0.082}]$			5.915
$Co_2Mn_{0.73}Fe_{0.67}Si_{0.84}$	III	$Co_{1.887}Mn_{0.059}Fe_{0.054}][Mn_{0.521}Fe_{0.479}][Si_{0.792}Mn_{0.108}Fe_{0.099}]$	0.5633	0.5645	6.028

Table III. Empirical formulas, SSFU composition types, SSFU compositions, measured lattice constants a and c, and Z_t-24 values of series-C CMFS films.

$Co_2Mn_\alpha Fe_\beta Si_{0.84}$ ($\beta' = 0.16$)	SSFU composition type	SSFU composition	a (nm)	c (nm)	Z_t-24
$Co_2Mn_{1.14}Fe_{0.16}Si_{0.84}$	III	$[Co_{1.932}Mn_{0.059}Fe_{0.008}][Mn_{0.877}Fe_{0.123}][Si_{0.812}Mn_{0.165}Fe_{0.023}]$			5.585
$Co_2Mn_{1.19}Fe_{0.16}Si_{0.84}$	III	$[Co_{1.909}Mn_{0.080}Fe_{0.011}] [Mn_{0.881}Fe_{0.119}][Si_{0.802}Mn_{0.175}Fe_{0.023}]$			5.566
$Co_2Mn_{1.24}Fe_{0.16}Si_{0.84}$	III	$[Co_{1.887}Mn_{0.100}Fe_{0.013}][Mn_{0.886}Fe_{0.114}][Si_{0.792}Mn_{0.184}Fe_{0.024}]$	0.5679	0.5666	5.547

Table IV. General expressions for SSFU compositions of $Co_2Mn_{\alpha'}Fe_{\beta'}Si_{\beta}$ from type I to type IV for $0 < \delta < 2$ and $0 < \beta < 2$; where, $\delta = \alpha'+\beta'$ and $\xi = \beta'/(\alpha'+\beta')$. The first, second, and third brackets in the SSFU composition of type III, $[Co_{2-x}(Mn_{1-\xi}Fe_{\xi})_x][(Mn_{1-\xi}Fe_{\xi})][Si_{1-y}(Mn_{1-\xi}Fe_{\xi})]$, represent the nominal Co, Mn/Fe, and Si sites.

SSFU composition type	Site-specific formula unit composition (SSFU composition)	x	y
I	$Co_2[(Mn_{1-\xi}Fe_{\xi})_{1-x-y}Co_xSi_y]Si$	$\dfrac{2(2-(\delta+\beta))}{2+\delta+\beta}$	$\dfrac{3\beta-(2+\delta)}{2+\delta+\beta}$
II	$Co_2[(Mn_{1-\xi}Fe_{\xi})_{1-x}Co_x][Si_{1-y}(Mn_{1-\xi}Fe_{\xi})_y]$	$\dfrac{2(2-(\delta+\beta))}{2+\delta+\beta}$	$\dfrac{2+\delta-3\beta}{2+\delta+\beta}$
III	$[Co_{2-x}(Mn_{1-\xi}Fe_{\xi})_x][Mn_{1-\xi}Fe_{\xi}][Si_{1-y}(Mn_{1-\xi}Fe_{\xi})_y]$	$\dfrac{2(\delta+\beta-2)}{2+\delta+\beta}$	$\dfrac{2+\delta-3\beta}{2+\delta+\beta}$
IV	$[Co_{2-x}(Mn_{1-\xi}Fe_{\xi})_x][(Mn_{1-\xi}Fe_{\xi})_{1-y}Si_y]Si$	$\dfrac{2(\delta+\beta-2)}{2+\delta+\beta}$	$\dfrac{3\beta-(2+\delta)}{2+\delta+\beta}$

Figure captions

FIG. 1. (Color online) Typical magnetic hysteresis curves for (a) series-A and (b) series-B CMFS films at 10 K measured using a SQUID magnetometer, where H was applied in the plane of the film along the $[1{-}10]_{CMFS}$ easy axis.

FIG. 2. (Color online) Typical dependence of $R_P A$, $R_{AP} A$, and TMR ratio on MgO barrier thickness (t_{MgO}) at 290 K for CMFS MTJs with $Co_2Mn_{1.24}Fe_{0.16}Si_{0.84}$ electrodes for a t_{MgO} range from 2.2 to 3.0 nm, where A is the junction area. The MgO tunnel barrier had a wedge structure, and its nominal thickness was varied from 1.4 to 3.2 nm on each 20×20 mm^2 substrate by linearly moving the shutter during the deposition by electron-beam evaporation.

FIG. 3. (Color online) (Mn+Fe) film composition dependence of the experimental saturation magnetization of series-A CMFS films at 10 K in comparison with (a) the Slater-Pauling value of $Z_t{-}24$ and (b) theoretical total spin magnetic moment per formula unit. (c) TMR ratio of MTJs with the corresponding CMFS films used as upper and lower electrodes as a function of (Mn+Fe) film composition [47].

FIG. 4. (Color online) Spin-projected local DOS (LDOS) per atom for (a) ordinary-site Mn ($Mn_{Mn/Fe}$), (b) ordinary-site Fe ($Fe_{Mn/Fe}$), (c) ordinary-site Co (Co_{Co}), and (d) antisite Co at the nominal Mn/Fe site ($Co_{Mn/Fe}$) for series-A CMFS ($Co_2Mn_{0.73}Fe_{\beta'}Si_{0.84}$).

FIG. 5. (Color online) Spin-projected total DOS per formula unit for (a) series-A CMFS ($Co_2Mn_{0.73}Fe_{\beta'}Si_{0.84}$ with a fixed α' of 0.73 in $Co_2Mn_{\alpha'}Fe_{\beta'}Si_{0.84}$ and various β' ranging from 0 to 0.67) and (b) series-B CMFS ($Co_2Mn_{\alpha'}Fe_{\beta'}Si_{0.84}$ with a fixed $\delta = \alpha' + \beta' = 1.40$ and various α' and β' ranging from $\alpha' = 0.73$ ($\beta' = 0.67$) to $\alpha' = 1.40$ ($\beta' = 0$))

FIG. 6. (Color online) Theoretically calculated local spin magnetic moments per atom, m_{spin}, for Mn, Fe and Co at the nominal Mn/Fe site ($Mn_{Mn/Fe}$, $Fe_{Mn/Fe}$, $Co_{Mn/Fe}$).

FIG. 7. (Color online) Experimental spin polarizations, P_{exp}, deduced from the TMR ratio at 4.2 K using a modified Julliere's model and two kinds of theoretical spin polarizations, $P_{th}(sp)$ and $P_{th}(spd)$, obtained by the KKR-CPA calculations as a function of $\delta = \alpha' + \beta'$ with $\alpha' = 0.73$ for series-A CMFS.

FIG. 8. (Color online) (Mn+Fe) film composition dependence of the experimental saturation magnetization of series-B CMFS films at 10 K in comparison with the Slater-Pauling value of $Z_t{-}24$ and theoretically calculated total spin magnetic moment, m_{spin}. (b) TMR ratio of series B CMFS MTJs as a function of β' with $\alpha' + \beta' = 1.40$ along with $Z_t{-}24$ on the top axis [47].

FIG. 9. (Color online) Experimental spin polarizations, P_{exp}, deduced from the TMR ratio at 4.2 K using a modified Julliere's model and two kinds of theoretical spin polarizations, $P_{th}(sp)$ and $P_{th}(spd)$, obtained by the KKR-CPA calculations as a function of β' with $\alpha' + \beta' = 1.40$ for series-B CMFS.

FIG. 10. (Color online) TMR ratios at (a) 4.2 K and (b) 290 K for CMFS/MgO/CMFS MTJs (CMFS MTJs) as a function of $\delta = \alpha' + \beta'$ in $Co_2Mn_{\alpha'}Fe_{\beta'}Si_{0.84}$ electrodes with $\beta' = 0.16$ ranging from 1.30 ($\alpha' = 1.14$) to 1.40 ($\alpha' = 1.24$). TMR ratios at (a) 4.2 K and (b) 290 K for identically fabricated CMS/MgO/CMS MTJs (CMS MTJs) as a function of α in $Co_2Mn_{\alpha}Si_{0.84}$ electrode are shown for comparison [47].
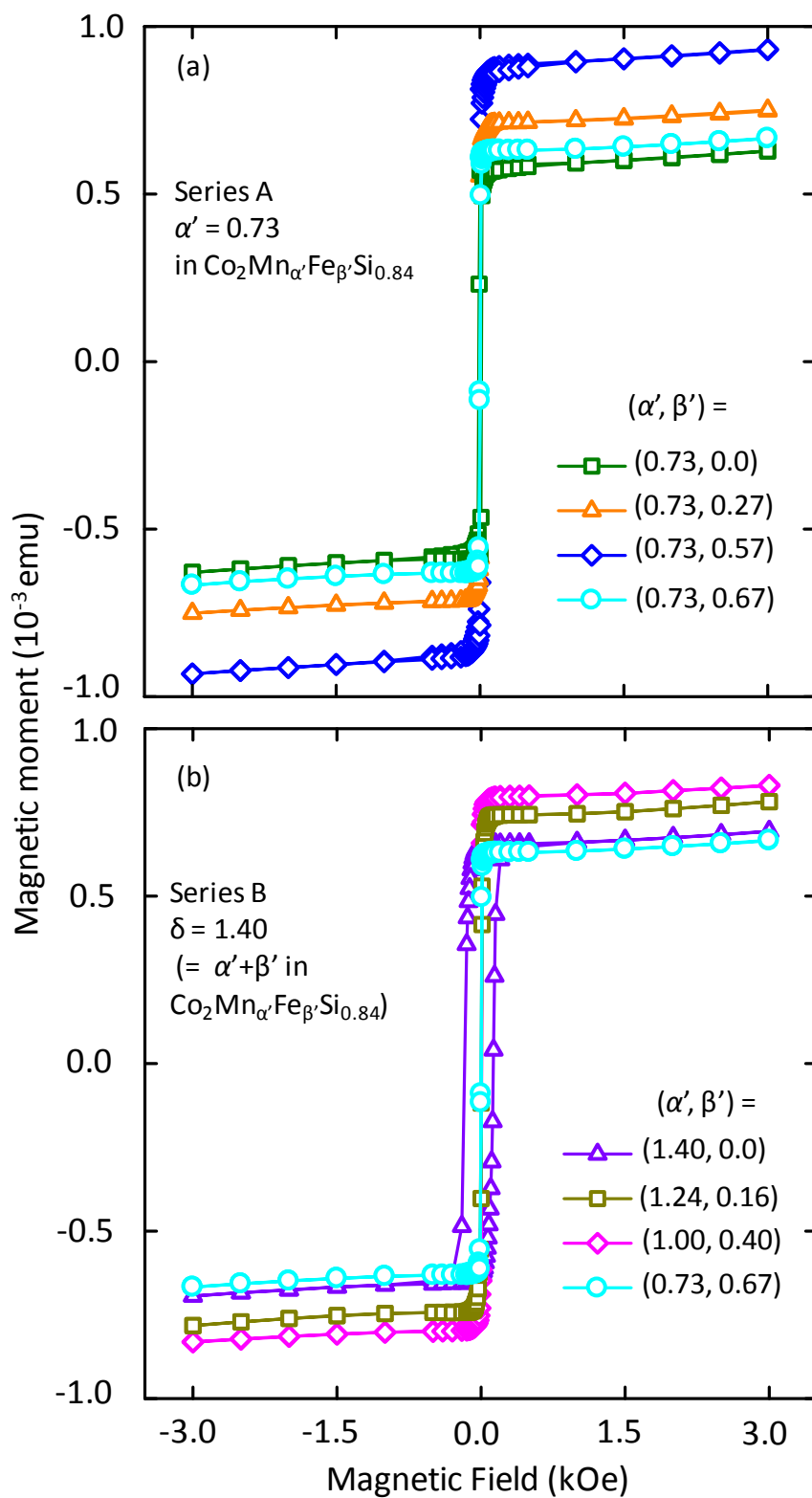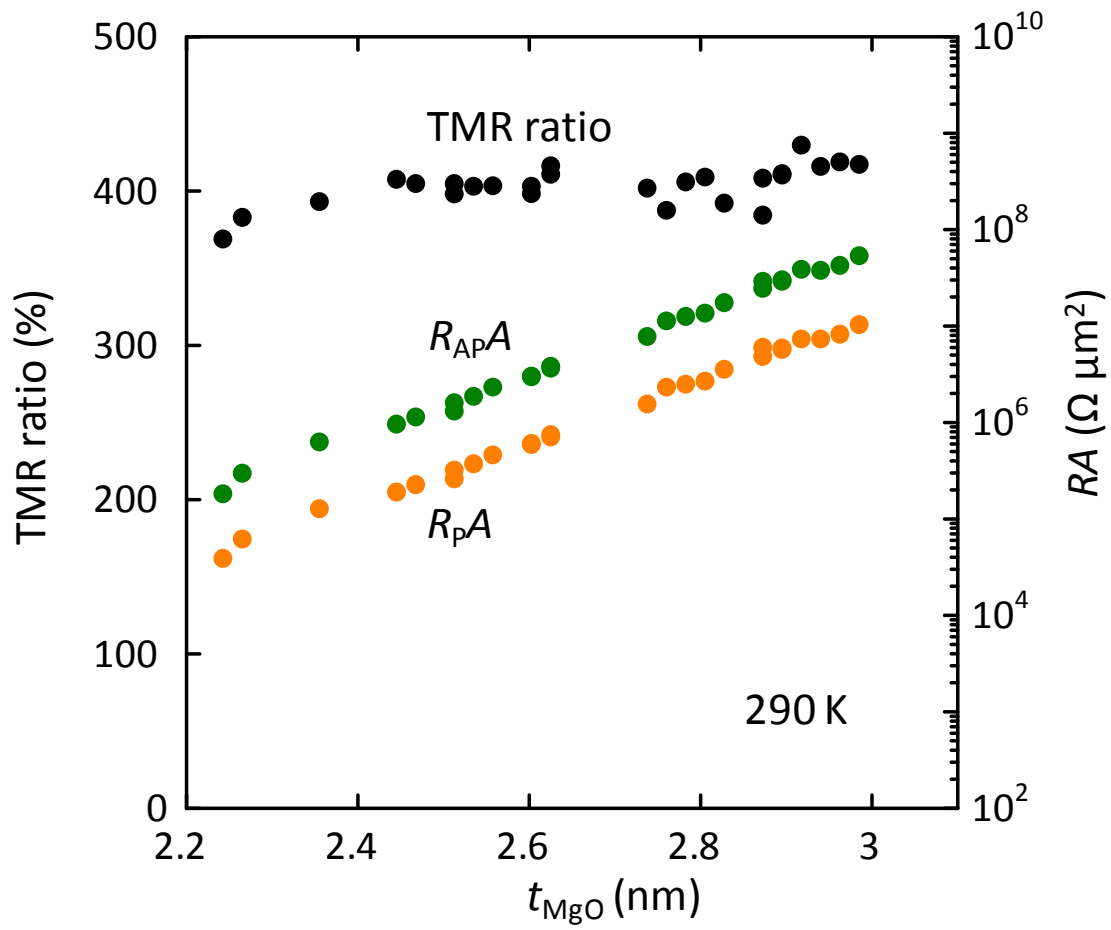
Fig. 1.

Fig. 2.

Fig. 3.

Fig. 4.

Fig. 5.
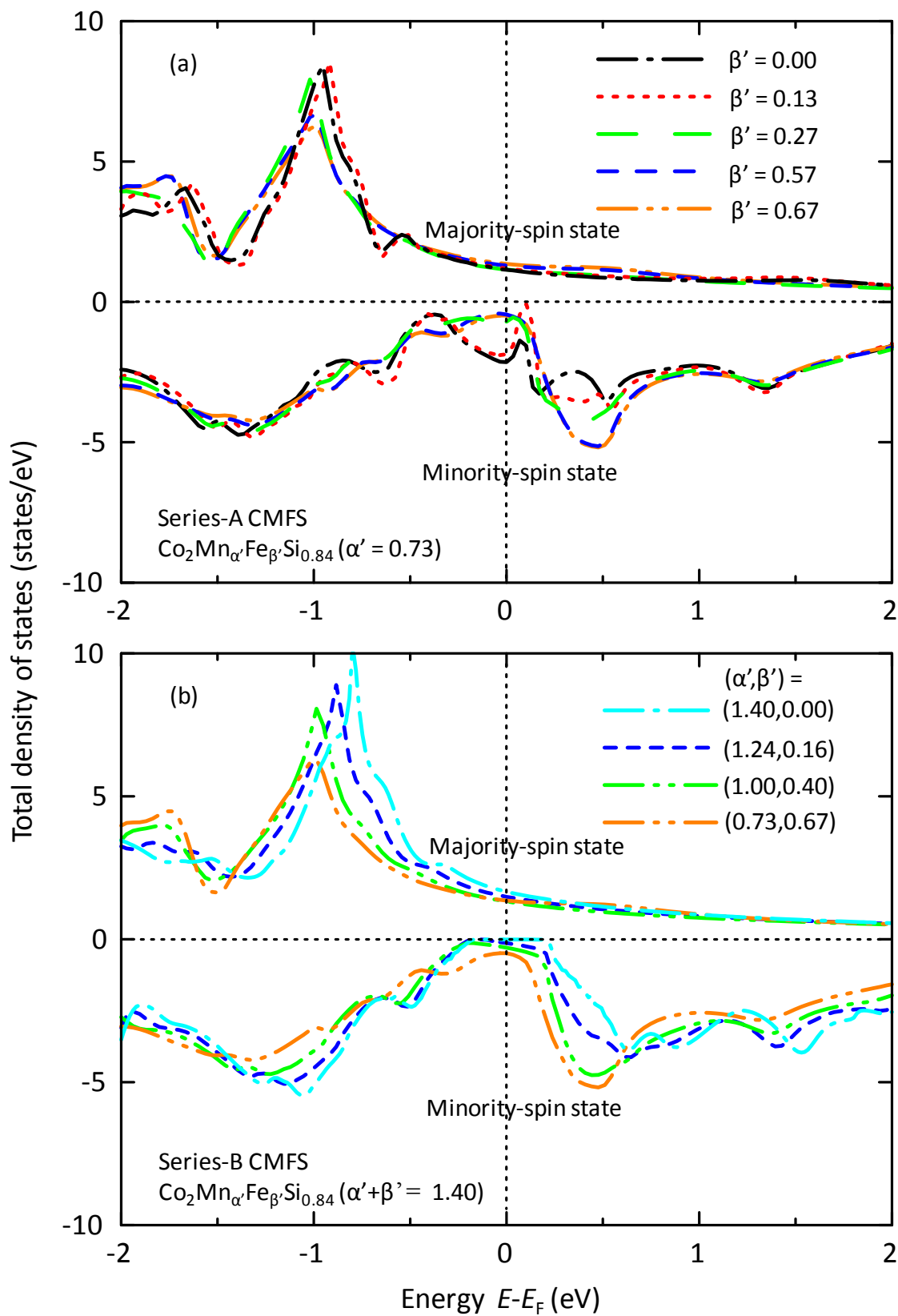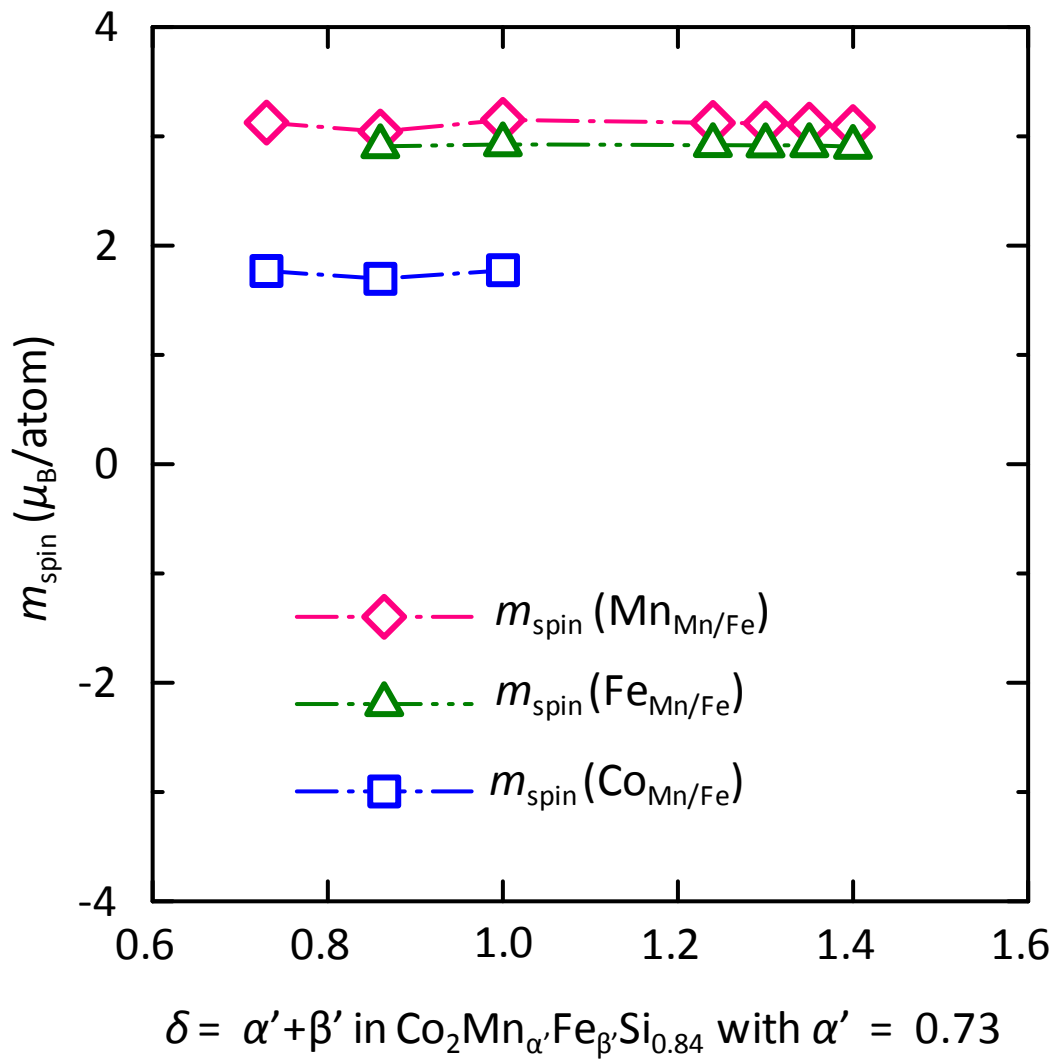
$\delta = \alpha' + \beta'$ in $Co_2Mn_{\alpha'}Fe_{\beta'}Si_{0.84}$ with $\alpha' = 0.73$

Fig. 6.

Fig. 7.

(a)

$Co_2Mn_{\alpha'}Fe_{\beta'}Si_{0.84}$ with $\alpha' + \beta' = 1.40$

Legend:
- - -◇- - - $Z_t{-}24$
- - -○- - - Experimental μ_s (μ_B/f.u.)
- - -△- - - Theoretical m_{spin} (μ_B/f.u.)

Y-axis: Experimental μ_s (μ_B/f.u), m_{spin}, $Z_t{-}24$

X-axis: β' in $Co_2Mn_{\alpha'}Fe_{\beta'}Si_{0.84}$ with $\alpha' + \beta' = 1.40$

(b)

$Z_t - 24$

2610% $(\alpha', \beta') = (1.24, 0.16)$

4.2 K

Region-a   Region-b

$\beta = 0$
$Co_2Mn_{1.40}Si_{0.84}$

$Co_2Mn_{\alpha'}Fe_{\beta'}Si_{0.84}$ with $\alpha'+\beta' = 1.40$

Y-axis: TMR ratio (%)

X-axis: β' with $\alpha'+\beta' = 1.40$

Fig. 8.

Fig. 9.

Fig. 10.

34